Applied Surface Science 317 (2014) 884–891

Contents lists available at ScienceDirect

Applied Surface Science

journal homepage: www.elsevier.com/locate/apsusc

A novel coating onto $LiMn_2O_4$ cathode with increased lithium ion battery performance

Jiesheng Zeng[a], Minsi Li[b], Xifei Li[a,*], Chen Chen[a], Dongbin Xiong[a], Litian Dong[a], Dejun Li[a,*], Andrew Lushington[c], Xueliang Sun[c,a]

[a] Energy & Materials Engineering Centre, College of Physics and Materials Science, Tianjin Normal University, Tianjin 300387, China
[b] Department of Chemistry, University of Science and Technology of China, Hefei, Anhui 230026, China
[c] Nanomaterials and Energy Lab, Department of Mechanical and Materials Engineering, Western University, London, Ontario N6A 5B9, Canada

ARTICLE INFO

Article history:
Received 21 May 2014
Received in revised form 8 August 2014
Accepted 8 August 2014
Available online 15 August 2014

Keywords:
$LiMn_2O_4$
MnO
Cycling performance
Mn dissolution

ABSTRACT

A sol–gel method was employed to synthesize $LiMn_2O_4$ cathode for lithium ion batteries. Calcination treatment with citric acid results in the reduction of external active materials of the cathode, finally a novel layer coating of MnO was proposed on the surface of $LiMn_2O_4$. The structures and morphologies of the as-prepared samples were characterized by XRD, Raman, SEM and HRTEM techniques. It was found that the reaction between $LiMn_2O_4$ and citric acid derived carbon occurred during coating process, and the resultant layer was verified to be MnO uniformly coated onto the cathode. Electrochemical performances show that the amount of coating exhibits a significant effect on $LiMn_2O_4$ performance, and the optimized MnO coating could exhibit improved battery performance of the $LiMn_2O_4$ cathode. The obtained improvement is attributed to decreased Mn dissolution into electrolyte upon cycling resulting from the MnO coating.

1. Introduction

Lithium ion batteries are a promising power source for a wide range of electronic applications including mobile phones and laptops. Furthermore, the high energy density and excellent cyclability of lithium ion batteries make them well suited for use in aerospace and electric vehicle applications [1–4]. Recently, spinel phase lithium-manganese oxide ($LiMn_2O_4$) has gained significant attention due to its low cost, low toxicity, minimal environmental impact [5–8]. However, $LiMn_2O_4$ undergoes severe capacity fading, which can be attributed to two main issues: (1) Jahn–Teller distortions occurring within the crystal lattice due to the electronic configuration of Mn^{3+}, $t_{2g}{}^3$–$e_g{}^1$ [9], and (2) increased surface reactivity between electrolyte and highly delithiated cathode material, leading to dissolution of Mn^{3+} into the electrolyte during the charge process [10]. Moreover, increasing the charge cutoff potential of $LiMn_2O_4$ may result in a dramatic increase of interfacial dissolution occurring [11]. Therefore, during the charge/discharge processes, $LiMn_2O_4$ cathode undergoes significant deterioration in cycling performance and rate capability, ultimately hindering its potential application in low-emission hybrid electric vehicle (HEV) and plug-in hybrid electric vehicle (PHEV) batteries.

In order to overcome these challenges, two strategies have been proposed to improve the electrochemical performance of the spinel $LiMn_2O_4$: (i) doping the spinel structure by replacing Mn, with Co, Zn, Fe, Ni, Cr, Ti, Ru, Mg, Al, etc. [12–15]; (ii) coatings on the spinel particles with $LiCoO_2$, organic polymer, SiO_2 [16], ZnO [17], $ZnMn_2O_4$ [18], etc. Recent publications have indicated that the coating method is particularly advantageous, resulting in $LiMn_2O_4$ demonstrating excellent performance [19]. To date, a variety of approaches have been reported to coat various materials on the cathodes [19–24]. Recently, our group applied ultrathin TiO_2, ZrO_2 and Al_2O_3 by atomic layer deposition onto $LiCoO_2$ material resulting in improved battery performance [19]. Thackeray et al. [20] demonstrated the use of a sol–gel technique to deposit amorphous ZrO_2, Al_2O_3 and SiO_2 coatings on $LiMn_2O_4$. Bai et al. [21] reported that the Y_2O_3-coated $LiMn_2O_4$ was prepared via precipitation method, the results showed that the 1 wt% Y_2O_3-coated $LiMn_2O_4$ electrode reveals excellent cycling performance with 80.3% and 76.7% capacity retention after 500 cycles at 1 C at 25 °C and 55 °C, respectively. Zhang et al. [22,23] have demonstrated a wet coating strategy to obtain LaF_3 and YPO_4 coatings. Another report by Kim et al. [24] have described that the Mn_2O_3 thin film prepared using a sol–gel method was coated onto the pristine $LiMn_2O_4$ cathode film through the

* Corresponding authors. Tel.: +86 13502042013; fax: +86 22 23766503.
E-mail addresses: xfli2011@hotmail.com, xli494@uwo.ca (X. Li), dejunli@mail.tjnu.edu.cn (D. Li).

http://dx.doi.org/10.1016/j.apsusc.2014.08.034
0169-4332/

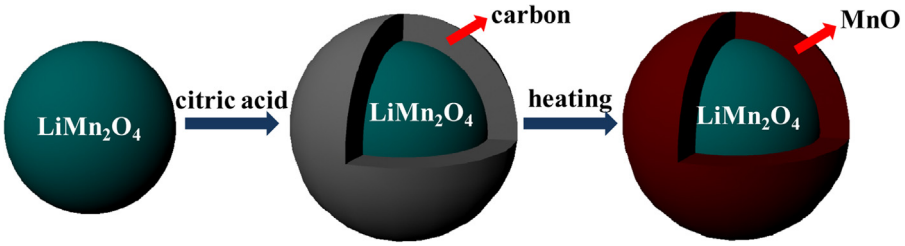

Scheme 1. Schematic illustration of the formation of a novel coating MnO on the spinel $LiMn_2O_4$.

annealing process. To a certain extent, the mentioned coatings above resulted in increased electrochemical performance. However, all aforementioned approaches are based on post-treatment coating processes, which typically have a weak adhesion between the coatings and the cathodes. Unlike post-treatment processes, the coating technique reported here offers the significant advantage of increased adhesion between coatings and cathodes, resulting in elevated electrochemical performance. Unfortunately, little work was reported to focus on this coating on the cathodes in lithium ion batteries.

In this study, we reported an innovative coating technique to enhance the cycling performance of the $LiMn_2O_4$ cathode. As described in Scheme 1, pristine powders were initially coated with a thin carbon film using citric acid as carbon source, these powders were then subsequently heated resulting in a novel coating layer (MnO) on the surface of active material. The MnO coating is proposed to be derived from $LiMn_2O_4$, leading to a strong adhesion between the coating and the cathode. It is expected that the MnO coating may serve as an active HF scavenger and prevent direct contact of HF acid with $LiMn_2O_4$ particles, resulting in increased cycling performance.

2. Experimental

$LiMn_2O_4$ was synthesized using stoichiometric amounts of lithium acetate (Acros, 98.5%), and manganese acetate (Acros, 99%)

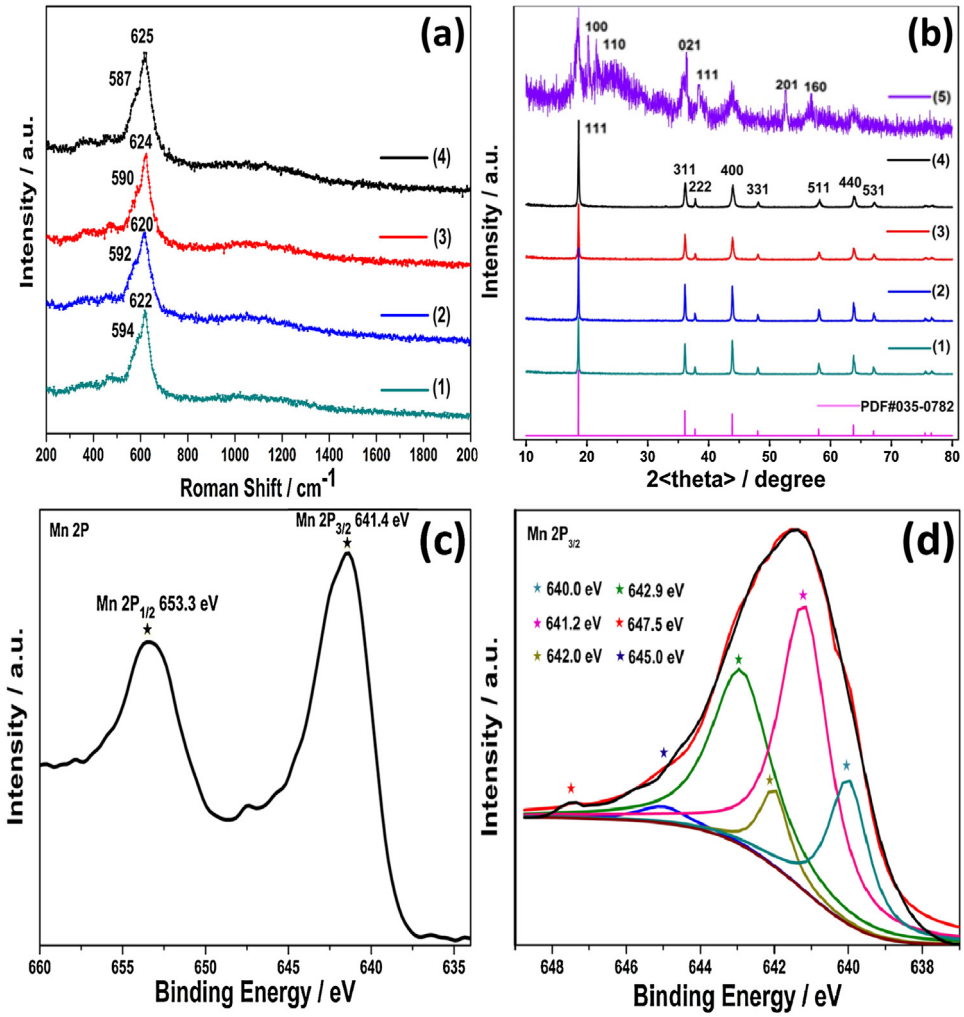

Fig. 1. (a) Raman spectra of (1) LMO-0, (2) LMO-10, (3) LMO-20, and (4) LMO-30. (b) XRD patterns of (1) LMO-0, (2) LMO-10, (3) LMO-20, (4) LMO-30, and (5) the cathode prepared by using over amount of citric acid. (c) XPS spectra of the Mn 2P special region for LMO-30. (d) The fitted Mn $2P_{3/2}$ spectrum.

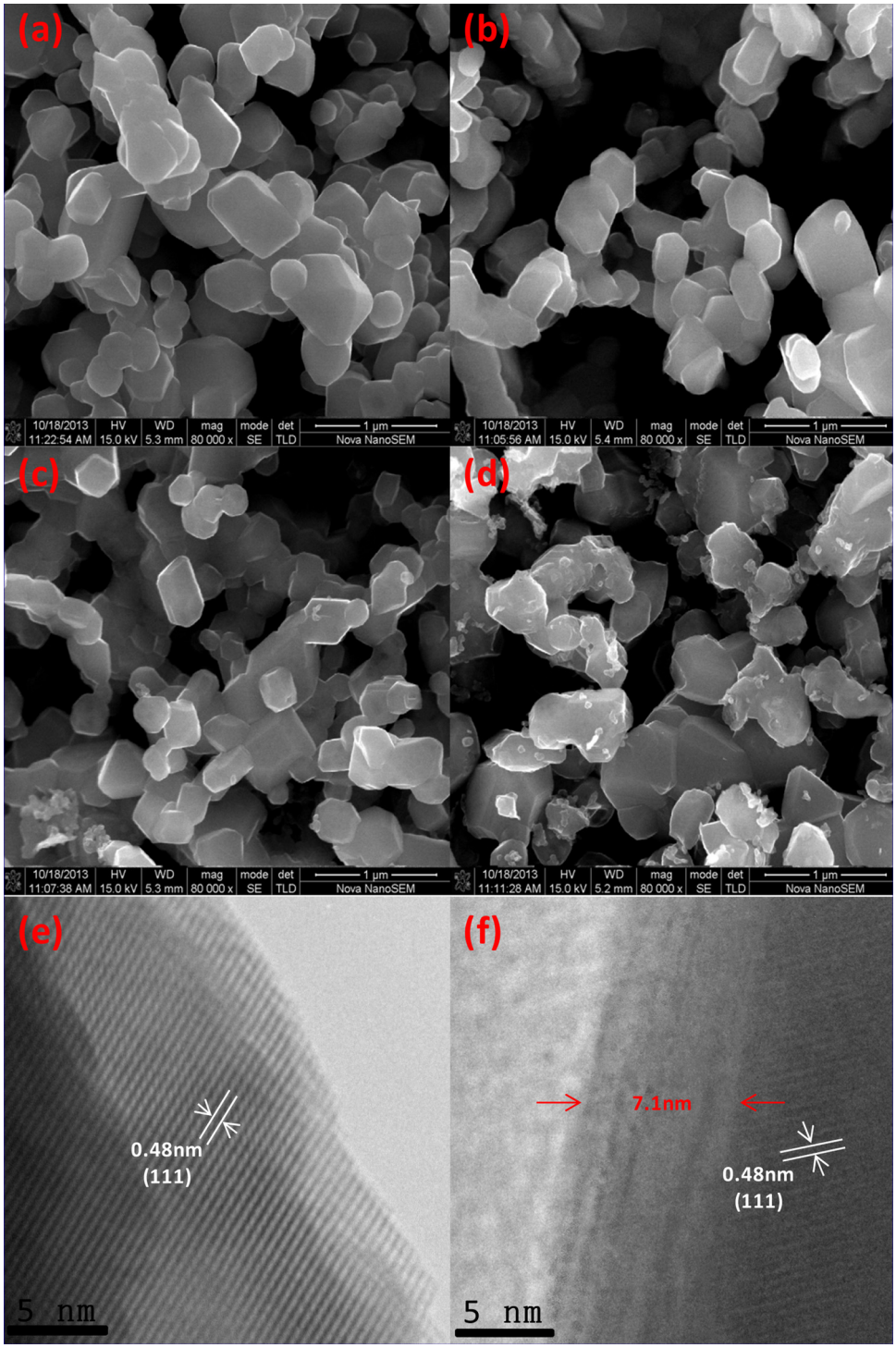

Fig. 2. SEM images of (a) LMO-0, (b) LMO-10, (c) LMO-20, and (d) LMO-30; HR-TEM lattice images of (e) LMO-0 and (f) LMO-30.

in a 1.03:2 molar ratio, respectively. These two materials were dissolved in distilled water, while citric acid was added in a molar ration of 1:1 with the total metal ions. After mild stirring, the pH value was adjusted to 7.0 with the slow addition of ammonium hydroxide. The solution was then heated at 80 °C with stirring. The resultant gel was dried in an oven for 48 h at 60 °C. The obtained powder was pre-heated at 450 °C for 5 h, and calcined at 750 °C for 10 h in air in a muffle furnace. After cooling to room temperature, the pristine $LiMn_2O_4$ sample which was labeled as LMO-0 was obtained.

The modified samples were prepared as follows, various concentration of citric acid (10%, 20%, and 30%) was dissolved in ethyl alcohol to which $LiMn_2O_4$ powder was added. These samples were labeled as LMO-10, LMO-20 and LMO-30, respectively. After sonication, the mixture was vigorously stirred for several hours and then dried at 70 °C for 4 h. The samples were finally calcined at 600 °C for 1 h in air.

The resultant material was ground into a fine powder using agate mortar. X-ray diffraction (XRD) was carried out to identify crystal structure of all the samples on a PANalytical's Empyrean

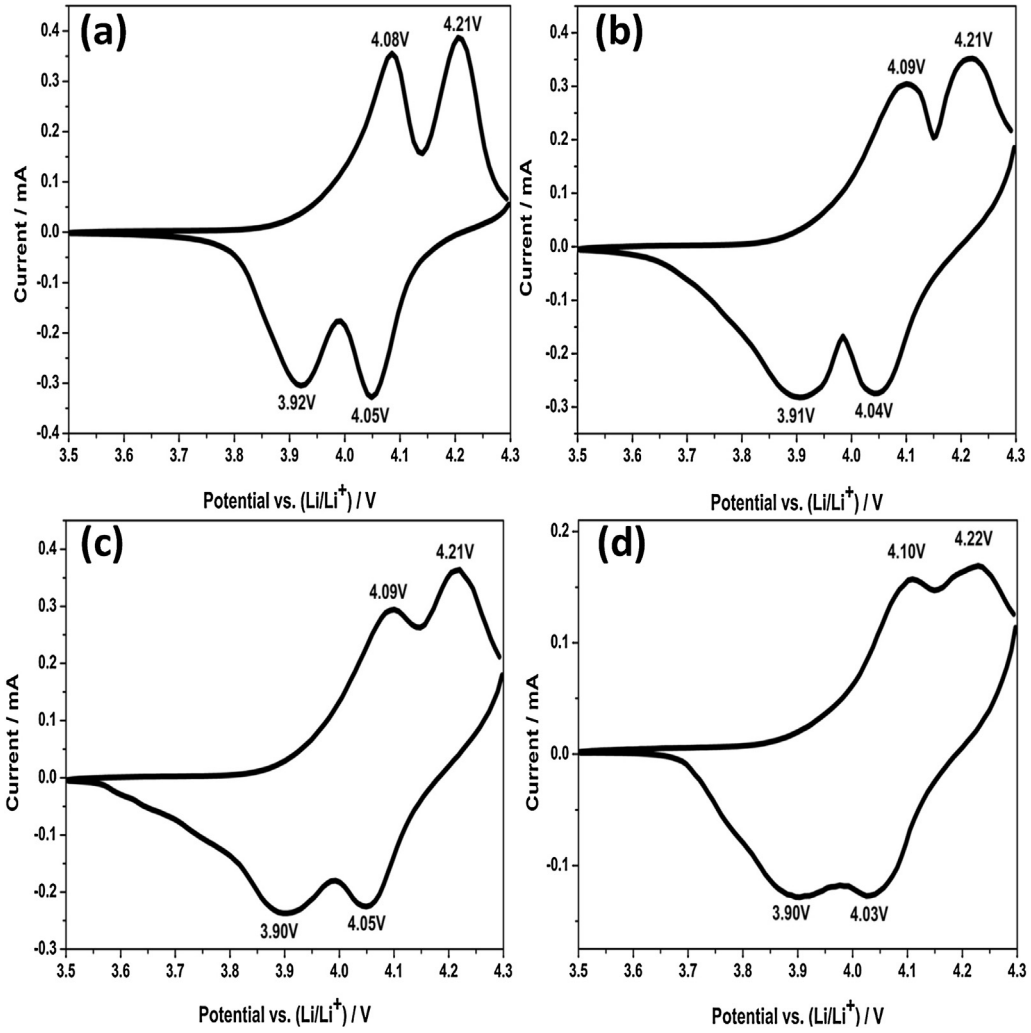

Fig. 3. Cyclic voltammograms of (a) LMO-0, (b) LMO-10, (c) LMO-20, and (d) LMO-30 in the voltage range of 3.5–4.3 V (vs. Li/Li^+) at a scanning rate of 0.1 mV s^{-1}.

unit with a Cu Kα radiation. The morphology was examined by Scanning electron microscopy (SEM) which was performed on a Nova NanoSEM. High resolution transmission electron microscopy (HRTEM) measurements were conducted by JEOL JEM-3000F. Raman spectra were recorded using LabRAM HR800 and XPS spectra were conducted by PHI5000VersaProbe.

The working electrodes were prepared by slurry-casting on 15 μm-thick Al foils that served as current collectors. The slurry contained 80 wt% the active materials, 10 wt% carbon black and 10 wt% polyvinylidene fluoride binder in the N-methylpyrrolidinone (NMP) solvent. The obtained electrodes were dried in a vacuum at 90 °C overnight.

The electrochemical performance of the materials was investigated using 2032 type coin cells. The coin cells were assembled in an argon-filled glove box (moisture and oxygen level less than 1.0 ppm). The $LiMn_2O_4$ electrodes and lithium foil were used as the working electrode and counter electrode, respectively. The electrolyte was composed of 1 M $LiPF_6$ salt dissolved in a 1:1 mass ratio of ethylene carbonate (EC) and dimethyl carbonate (DMC). The assembled cells were allowed aged for 12 h before electrical measurements were taken. Charge–discharge characteristics were galvanostatically tested between 3.5 and 4.3 V (vs. Li/Li^+) at room temperature using LANHE CT2001A. Cyclic voltammograms (0.1 mV s^{-1}; 3.5–4.3 V vs. Li/Li^+) and electrochemical impedance spectra (the frequency was varied from 0.1 MHz to 0.01 Hz with potential amplitude of 5 mV) were performed on Princeton Applied Research VersaSTAT 4.

3. Results and discussion

Raman spectra of LMO-0, LMO-10, LMO-20 and LMO-30 are presented in Fig. 1(a). The strong band at 624 cm^{-1} may be assigned to the A_{1g} mode corresponding to Mn—O stretching vibrations in MnO_6. The weak shoulder band at 592 cm^{-1} is assigned to the T_{2g} mode [25]. These two bands can also be found in all the ones that were treated with citric acid. Interestingly, no carbon signals related to G and D bands were observed. As it is designed, during the process of calcination treatment, the formed carbon which was decomposed onto the surface of cathode could fully react with the $LiMn_2O_4$ to produce a novel protective layer on the $LiMn_2O_4$ cathode [26].

The XRD patterns of LMO-0, LMO-10, LMO-20 and LMO-30 are shown in Fig. 1(b) with diffraction peaks appearing at $2\theta = 18.6°$, 36.1°, 37.7°, 43.9°, 48.0°, 58.1°, 63.8°, 67.1°, 75.5°, 76.5°, which can all be assigned to cubic spinel $LiMn_2O_4$ with the space group of Fd-3m (PDF#035-0782). Moreover, the sharp well defined Bragg lines correspond to a good spinel structure. Unfortunately, the existence of a secondary phase is negligible under the resolution utilized by the diffractometer due to the thinness of the coating. In order to further analyze the novel coating layer, a sample was

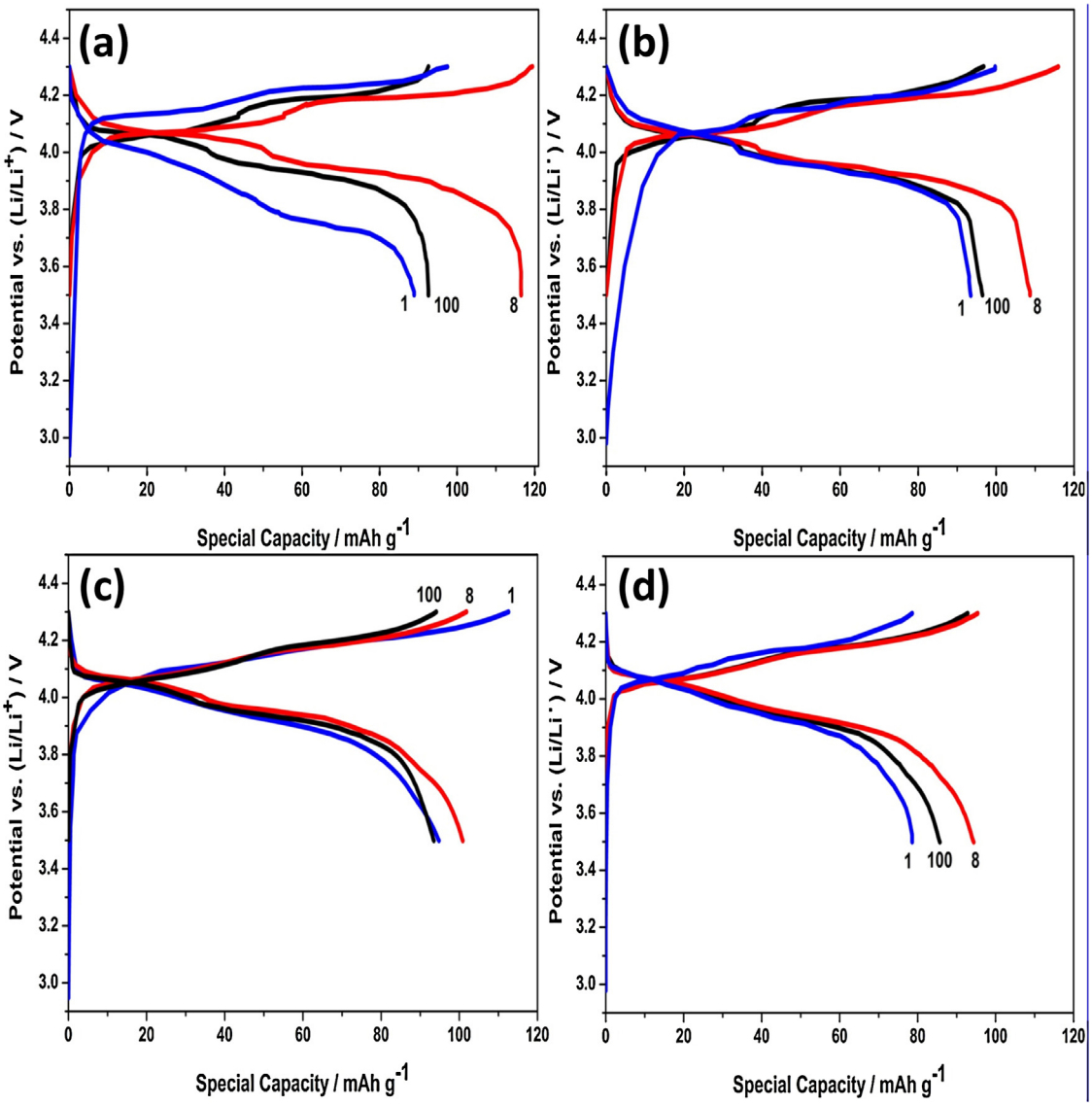

Fig. 4. Charge–discharge profiles of (a) LMO-0, (b) LMO-10, (c) LMO-20, (d) LMO-30 at different cycles at 1 C at room temperature.

prepared using an excessive amount of citric acid. The XRD pattern for this sample, as show in Fig. 1(b) (5), exhibits diffraction peaks at $2\theta = 20.2^\circ$, 21.5°, 36.3°, 38.2°, 52.5° and 56.7°, which are consistent with MnO. This provides confirmation that during the heating process a thin layer of MnO is formed due to carbon thermal reduction occurring at the surface of $LiMn_2O_4$ (see Scheme 1). As described above, the carbon layer which adhered to the surface of LMO particles was utmost thin. Therefore, just the external active materials of the electrode had been reacted with the carbon during the heating process, but the bulk of LMO inside was not affected completely, which can be confirmed in Fig. 1(b).

Fig. 1(c) and (d) presents the XPS spectra of LMO-30 for the Mn 2P spectral region and the fitted Mn $2P_{3/2}$ spectrum, respectively. The difference between the binding energy for Mn $2P_{1/2}$ and Mn $2P_{3/2}$ is called the spin-orbit splitting which is the characteristic of MnO, the value obtained here is 11.9 eV and in accord with other report [27]. Furthermore, the fitted Mn $2P_{3/2}$ spectrum Fig. 1(d) displays multiplet peaks at 640.0, 641.2, 642.0, 642.9, 647.5 eV and a satellite peak at 645.0 eV which can be attributed to Mn^{2+} in MnO [28].

Fig. 2(a)–(d) presents SEM images of pristine and modified $LiMn_2O_4$ samples. All samples display an agglomerated morphology with particle sizes ranging between 200 and 600 nm. As seen in Fig. 2(a), pristine $LiMn_2O_4$ demonstrates well-defined crystalline nature, however, after modification treatment an alternate morphology is observed with the appearance of burrs on the surface, as seen in Fig. 2(d). HR-TEM was employed, to determine the thickness of the novel coating. As shown in Fig. 2(e) and (f), HRTEM images of the pristine $LiMn_2O_4$ display clear a lattice profile with a *d*-value of 0.48 nm, corresponds to the hkl (1 1 1) plane of the spinel $LiMn_2O_4$. The images display homogeneous features outside and inside the particle with no alterations to the surface of $LiMn_2O_4$. As shown in Fig. 2(f), a difference can be clearly observed for the surface of LMO-30. That is a layer coating formation during the synthesis process, which was proved to be MnO based on the XRD and XPS results. Moreover, the formed layer was uniformly coated on the $LiMn_2O_4$ particle and the coating thickness is estimated about 7.1 nm.

Fig. 3(a)–(d) compares the CV profiles of the pristine and modified $LiMn_2O_4$ cycled between 3.5 and 4.3 V (vs. Li/Li^+), with a sweep rate of 0.1 mA s^{-1} at room temperature. Two redox peaks located at around 4.09/4.21 V and 3.91/4.05 V (vs. Li^+/Li) can be found

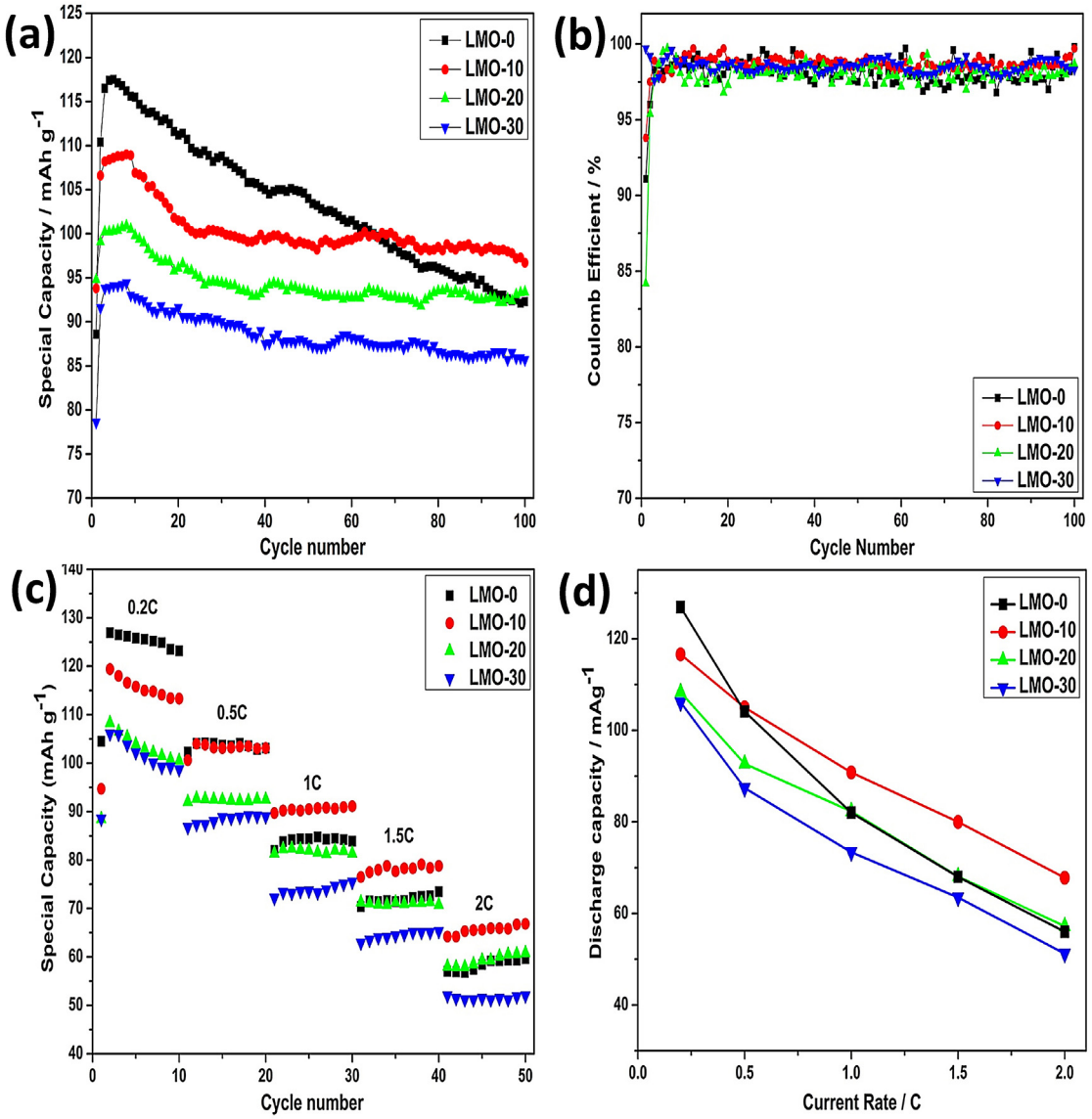

Fig. 5. (a) Cycling performance and (b) columbic efficiency vs. cycle number of LMO-0, LMO-10, LMO-20 and LMO-30 at 1 C rate between 3.5 and 4.3 V at room temperature; (c) rate capability of LMO-0, LMO-10, LMO-20 and LMO-30 at various current rates ranging from 0.2 C to 2 C (1 C = 148 mA g^{-1}); (d) the comparison of the discharge capacities of LMO-0, LMO-10, LMO-20 and LMO-30 electrodes at different discharge rate at room temperature, between 3.5 and 4.3 V.

for all samples and are characteristic of spinel $LiMn_2O_4$ [29,30]. Furthermore, the coupled redox peaks observed in the CV curves correspond to a two-step electrochemical processes where lithium ions are extracted and inserted from/into the spinel phase [31,32]:

$$LiMn_2O_4 \leftrightarrow Li_{1-x}Mn_2O_4 + x0.5Li^+ + x0.5e^- \quad (x < 0.5)$$

$$Li_{1-x}Mn_2O_4 \leftrightarrow 2MnO_2 + (1-x)Li^+ + (1-x)5e^- \quad (x > 0.5)$$

It can be seen that in all samples, the intensity of anodic peaks are higher than that of the cathodic peaks indicating that: (i) the coulombic efficiency is lower than 100%, and (ii) the anodic process is more facile and its process is diffusion with good reversibility [33]. In addition, there was almost no obvious difference in the separation of peak potentials in all CV curves of the samples, indicating that the modification process did not affect the lithium insertion and exaction process. However, the peak splitting observed in LMO-30 gives strong indication that a thick layer of MnO exists on that surface.

Fig. 4 presents charge–discharge curves of four samples at a current rate of 1 C (assuming 1 C = 148 mA g^{-1}) in a voltage rang of 3.5–4.3 V at room temperature. As observed in Fig. 4(a) and (b), two defined plateaus, one at the average potential of 4.10 V and the other at the average potential of 3.95 V, also verified the two-step electrochemical Li^+ insertion/extraction processes [18]. Interestingly, Fig. 4(d) demonstrates that as concentration of citric acid solution increases, the charge and discharge plateaus become less resolved. All samples exhibit a similar trend of obtaining the highest discharge capacity after several cycles due to an activation process. The capacity retention for LMO-0, LMO-10, LMO-20 and LMO-30 between the 8th and the 100th cycles was determined to be 79.5%, 88.8%, 92.7%, 90.8%, respectively. The modified $LiMn_2O_4$ typically exhibited a lower discharge capacities compared to LMO-0, but demonstrated higher capacity retention, up to 100 cycles, at 1 C. This is mainly because the pristine electrode LMO-0 was eroded by the electrolyte during the cycling, which resulted in serious capacity decay. However, as for the modified electrodes, after high temperature reaction between $LiMn_2O_4$ and the formed carbon, a coating layer MnO was formed on the active materials

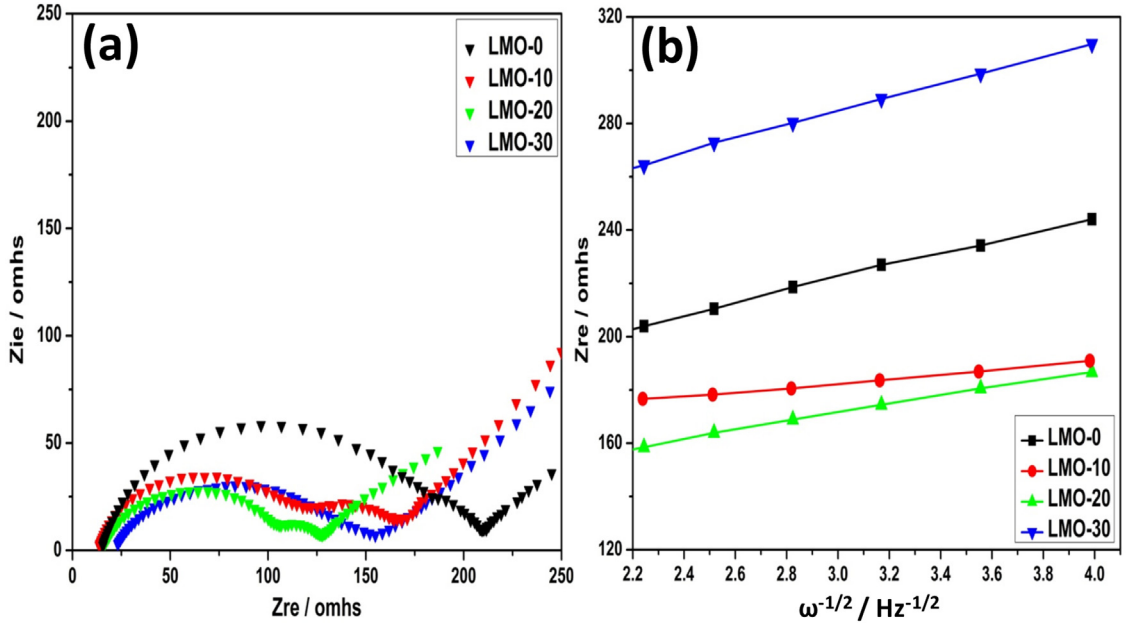

Fig. 6. (a) Electrochemical impedance spectra of LMO-0, LMO-10, LMO-20 and LMO-30 in the frequency range between 0.01 Hz and 0.1 MHz at 4.1 V during the first charge cycle; (b) the relationship between Z_{re} and $\omega^{-1/2}$ at low frequencies of LMO-0, LMO-10, LMO-20 and LMO-30.

to completely protect the electrodes from direct contact with the HF acid in the electrolyte as following: $MnO + 2HF \rightarrow MnF_2 + H_2O$, which suppresses dissolution of spinel into the electrolyte to obtain the better capacity retention [34].

Fig. 5(a) displays the cycling performance of LMO-0, LMO-10, LMO-20 and LMO-30 at a rate of 1 C in the voltage region of 3.5–4.3 V at room temperature. After activation in the first several cycles, the highest discharge specific capacities obtained for LMO-0, LMO-10, LMO-20, and LMO-30 were 117.5, 108.7, 100.9, 94.4 mA h g^{-1}, respectively. LMO-0 displayed the highest value, as compared to all modified samples. However, after 100 charge–discharge cycles, LMO-10 and LMO-20 exhibit a higher discharge capacity (96.5 and 93.5 mA h g^{-1}, respectively) with decreased capacity fade (0.13 and 0.08 mA h g^{-1} $cycle^{-1}$, respectively), when compared to LMO-0 (92.6 mA h g^{-1} and 0.25 mA h g^{-1} $cycle^{-1}$), demonstrating increased cycling performance. In particular, LMO-10 provided a relatively high discharge specific capacity of 108.7 mA h g^{-1} after electrochemical activation, and still maintained 88.8% of its capacity in the 100th cycle. Fig. 5(b) displays coulombic efficiency vs. cycle number. The data presented shows that during the first few cycle, the coulombic efficiency of LMO-0, LMO-10, LMO-20 and LMO-30 are relatively low, around 95%, which may be due to the formation of a solid electrolyte interphase (SEI) layer, preventing the electrode material from becoming fully activated. However, after several cycles, this values increases to the range of 97–100%.

Fig. 5(c) and (d) compare the rate capability of all the samples charged and discharged at a rate of 0.2–2 C (1 C = 148 mA g^{-1}) at room temperature. All samples displaying decreasing discharge capacity with increasing C-rate as a result of decrease Li-ion diffusion from the host $LiMn_2O_4$ particles [35]. LMO-0 displays the highest initial discharge capacity of 125 mA h g^{-1} at 0.2 C, but decreases rapidly with increasing current density. On the contrary, LMO-10 demonstrates slower capacity decay with increasing current rates, reaches high capacity of around 65 mA h g^{-1}. In addition, LMO-10 displays the highest discharge capacity at 1 C, 1.5 C and 2 C rates compared to LMO-0, LMO-20 and LMO-30. The improved performance observed for LMO-10 under elevated current rates may be because this coated sample was more resistive to electrolyte etching than LMO-0, furthermore, the appropriate amount of citric acid (10%) results in suitable thickness of coating film, which not only successfully protected the active material from erosion of electrolyte, but also allow the lithium ions migrate more freely to obtain relative high discharge capacity while in comparison with other modified samples [36].

Impedance spectral measurements can offer important elemental information upon cycling, such as electrolyte resistance, charge-transfer resistance and surface film. Fig. 6(a) shows the EIS of the cathode samples at a voltage of 4.1 V in the first charge cycle. The spectra consist of a single semicircle in the high frequency region, an arc in the middle frequency region, and a tail line in the low frequency region. The semicircle in the high frequency region is related to the migration of Li ions in the SEI layer, while the arc in the middle region originates from charge-transfer resistance. The line in the low frequency region is a result of Warburg impedance [37,38]. It is evident that the widths of the semicircle for modified $LiMn_2O_4$ are smaller than that found for LMO-0. This observation reflects that the impedance of modified $LiMn_2O_4$ samples, which were coated by a novel MnO layer, is less than that of LMO-0. This higher impedance seen for LMO-0 can be attributed to the increased capacity fade seen with increasing cycling, as observed in the samples cycling performance and rate capability. In addition, a plot of Z_{re} vs. the reciprocal square root of lower angular frequencies ($\omega^{-1/2}$) of LMO-0, LMO-10, LMO-20 and LMO-30 is plotted and presented in Fig. 6(b). The slope of the linear fit corresponds to the Warburg coefficient, and the lower value indicates the faster diffusion rate of Li ions on the surface of electrode [39,40]. This data indicates that line slope of LMO-10 is the lowest, which also proves that its electrode electrochemical polarization is the lowest during the charge–discharge cycling.

As mentioned earlier, spinel $LiMn_2O_4$ undergoes severe deterioration as a result of Mn^{3+} dissolution into the electrolyte during the charge/discharge process. In this research, a reduction of activity materials process was proposed to coat a novel layer MnO on the surface of $LiMn_2O_4$ cathode, more importantly, this approach results in excellent adhesion between the coating and the cathode. The resultant coating serves as an active HF scavenger and decreases the local concentration of HF acid near the $LiMn_2O_4$ surface as following: $MnO + 2HF \rightarrow MnF_2 + H_2O$. The novel coating

prevents $LiMn_2O_4$ particles from direct contact with HF acid in the electrolyte, resulting in reduced Mn^{3+} dissolution into the electrolyte. As is seen in Fig. 6, during charge–discharge cycling the novel coating decreases the impedance value of the cathode and the electrode electrochemical polarization. Therefore, the novel MnO coating increases the cycling performance and rate capability of the $LiMn_2O_4$ cathode.

4. Conclusions

For the first time we report a novel coating process to coat MnO on spinel $LiMn_2O_4$. The homogeneous layer of MnO provided enhanced protection against interfacial side reactions from occurring between $LiMn_2O_4$ surface and the electrolyte. The coating also effectively suppressed the dissolution of Mn^{3+} ion into the electrolyte. Moreover, since the surface coating was a result of a reaction between carbon and $LiMn_2O_4$, the obtained layer demonstrated a strong adhesion to the surface of the material. Electrochemical testing determined that LMO-10 exhibited the best cycling performance, compared to LMO-0, LMO-20 and LMO-30. Up to 100 cycles at 1 C rate, LMO-10 showed relatively high discharge specific capacity but only 0.13 mA h g^{-1} decay per cycle. Moreover, LMO-10 delivered the best rate capability when discharged at various current rates. It is found that the novel coating layer helped to reduce the impedance value, and the increased cycle performance was confirmed. This convenient and successful modified method proposed in this study shows some promising application in enhancing lithium ion battery performance.

Acknowledgements

This research was supported by Key Project of Tianjin Municipal Natural Science Foundation of China (14JCZDJC32200 and 13JCZDJC33900), National Natural Science Foundation of China (51272176 and 51472180), LPMT, CAEP (KF14006 and ZZ13007), Project 2013A030214 supported by CAEP, Science & Technology Department of Sichuan Province (2013GZX0145-3), and the program of Thousand Youth Talents in Tianjin of China.

References

[1] X. Fang, M.Y. Ge, J.P. Rong, C.W. Zhou, J. Mater. Chem. A 1 (2013) 4083–4088.
[2] J.M. Tarascon, M. Armand, Nature 414 (2001) 359–367.
[3] M. Armand, J.M. Tarascon, Nature 451 (2008) 652–657.
[4] T.H. Kim, J.S. Park, S.K. Chang, S. Choi, J.H. Ryu, H.K. Song, Adv. Energy Mater. 2 (2012) 860–972.
[5] M.M. Thackeray, M.F. Mansuetto, J.B. Bates, J. Power Sources 68 (1997) 153–158.
[6] X.F. Li, Y.L. Xu, Appl. Surf. Sci. 21 (2007) 8592–8596.
[7] F.W. Jeffrey, J. Power Sources 195 (2010) 939–954.
[8] G. Amatucci, J.M. Tarascon, J. Electrochem. Soc. 149 (2002) K31–K46.
[9] X.F. Li, Y.L. Xu, C.L. Wang, J. Alloys Compd. 1–2 (2009) 310–313.
[10] D.H. Jang, Y.J. Shin, S.M. Oh, J. Electrochem. Soc. 143 (1996) 2204–2211.
[11] X.F. Li, J. Liu, M.N. Banis, A. Lushington, R. Li, M. Cai, X.L. Sun, Energy Environ. Sci. 2 (2014) 768–778.
[12] M.V. Reddy, S.S. Manoharan, J. John, B. Singh, G.V. Subba Rao, B.V.R. Chowdari, J. Electrochem. Soc. 156 (2009) A652–A660.
[13] C. Polo Fonseca, M.A. Bellei, F.A. Amaral, S.C. Canobre, S. Neves, Energy Convers. Manage. 50 (2009) 1556–1562.
[14] T. Shiratsuchi, S. Okada, T. Doi, J.I. Yamaki, Electrochim. Acta 54 (2009) 3145–3151.
[15] R. Thirunakaran, A. Sivashanmugam, S. Gopukumar, R. Rajalakshmi, J. Power Sources 187 (2009) 565–574.
[16] Z.S. Zheng, Z.L. Tang, Z.T. Zhang, W.C. Shen, Y.S. Lin, Solid State Ionics 2 (2002) 148–317.
[17] H. Liu, C. Cheng, Z.Q. Hu, J. Mater. Sci. 40 (2005) 5767–5769.
[18] X.F. Li, Y.L. Xu, J. Solid State Electrochem. 7–8 (2008) 851–855.
[19] X.F. Li, J. Liu, X.B. Meng, T.J. Tang, M.N. banis, J.L. Yang, Y.H. Hu, R.Y. Li, M. Cai, X.L. Sun, J. Power Sources 1 (2014) 57–69.
[20] J.S. Kim, C.S. Johnson, J.T. Vaughey, S.A. Hackney, K.A. Walz, W.A. Zeltner, M.A. Anderson, M.M. Thackeray, J. Electrochem. Soc. 151 (2004) A1755–A1761.
[21] B.W. Ju, X.Y. Wang, C. Wu, Q.L. Wei, X.K. Yang, H.B. Shu, Y.S. Bai, J. Solid State Electrochem. 18 (2014) 115–123.
[22] S. Zhao, Q.J. Chang, K. Jiang, Y. Bai, Y.Q. Yang, W.F. Zhang, Solid State Ionics 253 (2013) 1–7.
[23] S. Zhao, Y. Bai, L.H. Ding, B. Wang, W.F. Zhang, Solid State Ionics 247 (2013) 22–29.
[24] J.H. Lee, K.J. Kim, Electrochim. Acta 102 (2013) 196–201.
[25] C. Julien, M. Massot, Mater. Sci. Eng. B 97 (2003) 217–230.
[26] H.J. Yue, X.K. Huang, D.P. Lv, Y. Yang, Electrochim. Acta 54 (2009) 5363–5367.
[27] M.A. Langell, C.W. Hutchings, G.A. Carson, M.H. Nassir, J. Vac. Sci. Technol. A 14 (1996) 1656–1661.
[28] H.W. Nesbitt, D. Banerjee, Am. Mineral. 83 (1998) 305–315.
[29] Y.Y. Xia, M. Yoshio, J. Electrochem. Soc. 143 (1996) 825–830.
[30] T. Ohzuku, M. Kitagawa, T. Hirai, J. Electrochem. Soc. 137 (1990) 40–46.
[31] X.Q. Yang, X. Sun, S.J. Lee, J. McBreen, S. Mukerjee, M.L. Daroux, X.K. Xing, Electrochem. Solid State Lett. 2 (1999) 157–160.
[32] Y.Y. Xia, M. Yoshio, J. Electrochem. Soc. 143 (1996) 825–833.
[33] R. Thirunakaran, R. Ravikumar, S. Gopukumar, A. Sivashanmugam, J. Alloys Compd. 556 (2013) 266–273.
[34] H. Liu, L.J. Fu, H.P. Zhang, J. Gao, Y.P. Wu, Electrochem. Solid-State Lett. 9 (2012) 529–533.
[35] M. Prabu, M.V. Reddy, S. Selvasekarapandian, G.V. Subba Rao, B.V.R. Chowdari, Electrochim. Acta 88 (2013) 745–755.
[36] C.H. Jiang, S.X. Dou, H.K. Liu, M. Ichihara, H.S. Zhou, J. Power Sources 173 (2007) 410–415.
[37] D. Arumugam, G.P. Kalaignan, Electrochim. Acta 55 (2010) 8709–8716.
[38] K.A. Striebel, E. Sakai, E.J. Cairns, J. Electrochem. Soc. 149 (2002) 61–68.
[39] D.E. Smith, Anal. Biochem. 38 (1966) 347–351.
[40] Y. Cui, X.L. Zhao, R.S. Guo, Electrochim. Acta 55 (2010) 922–926.